



Multiscale analysis of fine slag from pulverized coal gasification in entrained-flow bed

Lirui Mao^{1,2} · Mingdong Zheng^{2,3} · Baoliang Xia² · Facun Jiao² · Tao Liu² · Yuanchun Zhang² · Shengtao Gao² · Hanxu Li²

Received: 11 August 2022 / Accepted: 21 November 2023
© The Author(s) 2024

Abstract

Fine slag (FS) is an unavoidable by-product of coal gasification. FS, which is a simple heap of solid waste left in the open air, easily causes environmental pollution and has a low resource utilization rate, thereby restricting the development of energy-saving coal gasification technologies. The multiscale analysis of FS performed in this study indicates typical grain size distribution, composition, crystalline structure, and chemical bonding characteristics. The FS primarily contained inorganic and carbon components (dry bases) and exhibited a "three-peak distribution" of the grain size and regular spheroidal as well as irregular shapes. The irregular particles were mainly adsorbed onto the structure and had a dense distribution and multiple pores and folds. The carbon constituents were primarily amorphous in structure, with a certain degree of order and active sites. C 1s XPS spectrum indicated the presence of C–C and C–H bonds and numerous aromatic structures. The inorganic components, constituting 90% of the total sample, were primarily silicon, aluminum, iron, and calcium. The inorganic components contained Si–O–Si, Si–O–Al, Si–O, SO₄²⁻, and Fe–O bonds. Fe 2p XPS spectrum could be deconvoluted into Fe 2p_{1/2} and Fe 2p_{3/2} peaks and satellite peaks, while Fe existed mainly in the form of Fe(III). The findings of this study will be beneficial in resource utilization and formation mechanism of fine slag in future.

Keywords Coal gasification · Fine slag · Multiscale analysis · Carbon components · Inorganic components

1 Introduction

In September 2020, China predicted that its CO₂ emissions will peak by 2030 (China Government Network 2021). Energy storage technologies are yet to develop completely, and a major proportion of the energy requirements is still met using fossil fuels. Accordingly, it is urgent to realize the efficient and clean utilization of coal (Yang 2022; Chai 2021). Coal gasification technology is one of the main methods in this regard (Wang 2021a, b; Cao 2021; Ding et al. 2022; Smolinski et al. 2022; Zhakupov et al. 2022). However, gasification generates a large amount of solid

waste, known as fine slag (FS), which is usually disposed in landfills and causes environmental pollution. This limits the development of energy-efficient coal gasification technologies. Nonetheless, the inadequate utilization of the high residual carbon content in this FS is a waste of resources (Liu 2021).

Figure 1 presents the process for producing FS in a Shell gasifier. Raw coal particles enter the gasifier and undergo rapid pyrolysis. In this process, the raw coal particles undergo expansion and rupture, carbon matrix particles are consumed, and tiny ash particles are formed. Some of the particles on the gasifier wall collected from the molten slag stream downwards along the furnace wall and settle into the slag removal system. In the slag removal system, molten slag disintegrates into solid particles of various sizes. In industries, this portion of solid particles is known as coarse slag. The other portion of the particulates moves from the top of the gasifier to the raw synthetic gas. The fly ash generated from washing or trapped by dust removal devices is captured by the ceramic filter. The untrapped parts passes to mix into the black water in the cooling chamber and is transferred to

✉ Lirui Mao
maolirui123@163.com

¹ School of Chemical Engineering, Anhui University of Science and Technology, Huainan 232001, China

² School of Earth and Environment, Anhui University of Science and Technology, Huainan 232001, China

³ Institute of Energy, Hefei Comprehensive National Science Center, Hefei 230031, China

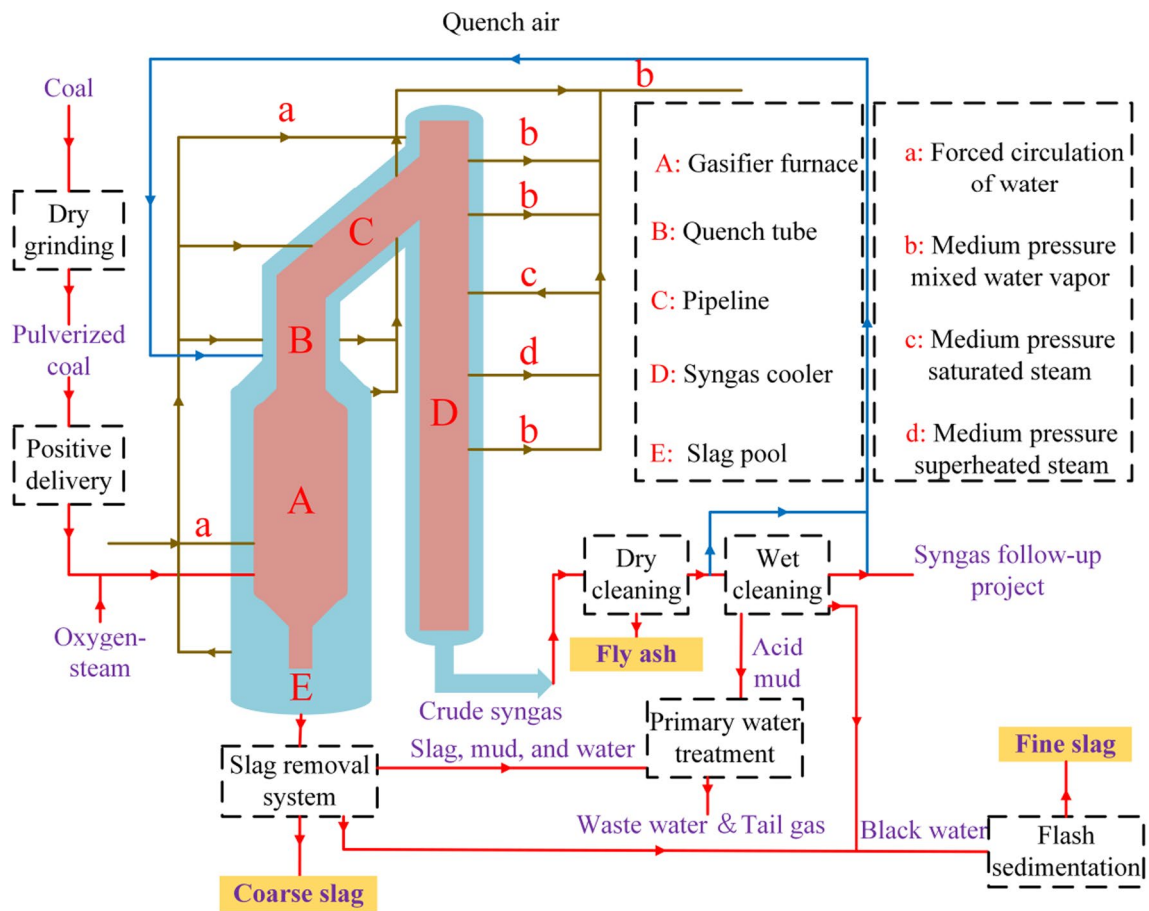


Fig. 1 Schematic of Shell coal gasification

the filter press to form the FS after an empty flash (Wang 2021a, b; Shen 2021; Zhao 2010).

Research on FS is mainly focused on its physical and chemical properties. The FS mainly contains SiO_2 , Al_2O_3 , CaO , and Fe_2O_3 (Lv 2021). The inorganic components include crystalline components (silicate, aluminosilicate, calcium, iron, and iron oxide) and glass components (calcium aluminosilicate glass) (Wu 2015). FS particles with different sizes have different characteristics, mainly because they undergo different processes in the gasifier. The breakdown of particulates, agglomeration of ash, and slag deposition should be considered (Pan 2016). Xu (2009) found that the inorganic substances were primarily spherical, while the residual carbon existed in a free flocculated form. Miao (2020a, b, c) demonstrated that the rich ore particles in the FS comprised abundant particles with small pores and a small number of solid particles with large pores. The large pores were independent of each other within the particles, and there were cracks, holes, and circular holes on the surface of the particles.

To further reveal the structural characteristics of the FS, many researchers have focused on the chemical structures

of the residual carbon and inorganic components in the FS. In addition to the discrete residual carbon particles in the FS, there are two other types of residual carbon particles. In the first type, the residual carbon particles form a matrix of rich ore particulates, while in the second type, the residual carbon is chemically and physically bound to inorganic matter in a rich granular matrix. The most important chemical bonds of the residual carbon in the rich granular matrix are C–C, C–H, and C–O. C–O combines with inorganic elements in the rich mineral particulate matter to form C–O–M groups (M represents inorganic elements) (Miao 2020a, b, c). Thus, there might be a specific relationship between the amounts of inorganic constituents and residual carbon in the FS. Melting test of the fine carbon slag mixture confirmed that the inorganic components tended to agglomerate into larger carbon-free spheres when melted in the carbon matrix (Miao 2020a, b, c). The smelting phase formed by the particles of the ore-rich materials in the gas generator covered the carbon materials in the particles (Krishnamoorthy 2017). The fate of coal particles can be analyzed in terms of coal migration, drywall interaction, coal deposition, and heterogeneous gasification response (Troiano 2018).

Thus, coal gasification is a complex process, and many factors influence the formation of the FS. The pressure and temperature fluctuations in an actual operation of the gasifier affect the morphology of the FS. The mechanism of interaction between the residual carbon and inorganic components of the FS is still elusive, and there is no suitable method to explain the formation of FS in the furnace. In this regard, it is necessary to analyze the macroscopic and microscopic morphological characteristics of the FS, which will be beneficial for the resource utilization of FS and the operation efficiency of gasification plants. This was one of the prime objectives of our study—we collected FS from actual factories, and the features of the FS were analyzed at the macroscopic and microscopic scales. The macrostructure and microstructure highlight the multiscale morphological characteristics of the FS. We also speculated the possible mechanism of FS formation based on the characteristics of FS. Additionally, the application prospects and contribution of the analysis of these multiscale factors of the FS are presented.

2 Experimental

2.1 Samples preparation

Different FS specimens were collected at a sampling interval of 2 h and evenly mixed to obtain the test samples. Table 1 shows the proximate and ultimate analysis of FS. Five specimens of FS (FS1#, FS2#, FS3#, FS4#, and FS5#) are obtained from a Shell gasifier in China. The gasification unit was in regular operation. The immediate and final analyses of the FS samples revealed the presence of numerous inorganic and carbon components. After comparing the properties of different FS, we selected FS1#, FS2#, and FS3# for further characterization at different scales. FS was burned to a constant weight at 815 °C to produce the ash of fine slag (FSA).

Various components of FSA are present as oxides. The highest content is that of SiO₂, followed by Al₂O₃, CaO,

and Fe₂O₃. MgO, Na₂O, K₂O, and P₂O₅ are present in small amounts. The oxide contents are shown in Fig. 2. Simultaneously, we analyzed the chemical composition of the coal ash in the raw coal (RC) formed during the operation of the gasifier. There is a correspondence between RC and FS. Analysis of the chemical composition of the raw coal ash (RCA) indicates enrichment of the iron content in the FS.

2.2 Experiment

The FS is pretreated with the aim of sufficiently dispersing the particles, and the pre-processing was divided into three steps:

Step 1: Addition of 100 g of FS in 200 g of anhydrous ethanol.

Step 2: Ultrasonic treatment for 2 h.

Step 3: Drying at 40 °C for 8 h in a nitrogen atmosphere.

The physical and chemical properties of the pre-processed FS were characterized at the macroscopic and microscopic scales. The experimental flowchart is shown in Fig. 3.

2.2.1 Macroscopic characterization

For macroscopic characterization of the FS, the particle size distributions and apparent morphologies were examined. The particle size was analyzed using a laser particle size analyzer. FS (50 mg) was completely dispersed in alcohol (dispersant) and placed into the instrument for analysis. The particle size distribution was determined from the average of three experiments. The repeatability error and accuracy error were < 1%.

The apparent morphology of the FS was analyzed by Scanning Electron Microscopy (SEM, FlexSEM1000, Hitachi, Japan). The sample was evenly distributed over a conductive adhesive, covered with a conductive film, and placed in the sample chamber. The sample chamber was vacuumed, and a high voltage was applied during the experiment. Typical characteristics were analyzed at various magnifications. ImageJ was used to analyze the images and determine the dimensions of the species.

Table 1 Proximate and ultimate analysis of FS*

Samples	Proximate analysis (wt%)			Ultimate analysis (wt%)					Calorific value (MJ/kg)
	A	V	FC**	C	H	O***	N	S	
FS1#	42.95	2.72	54.33	52.69	0.38	1.18	0.54	2.25	12.703
FS2#	34.10	1.25	64.65	62.92	0.26	0.37	0.60	1.74	13.613
FS3#	37.81	1.61	60.58	59.30	0.26	0.24	0.59	1.80	12.918
FS4#	38.14	1.10	60.76	60.23	0.34	0.42	0.12	0.75	13.215
FS5#	42.22	1.41	56.73	55.93	0.30	0.25	0.25	1.05	11.523
Repeatabilit	±0.50%	±0.30%	—	±0.50%	±0.15%	—	±0.08%	±0.10%	±0.15%

*Dry basis (40 °C-8 h). **Minusing. ***Minusing

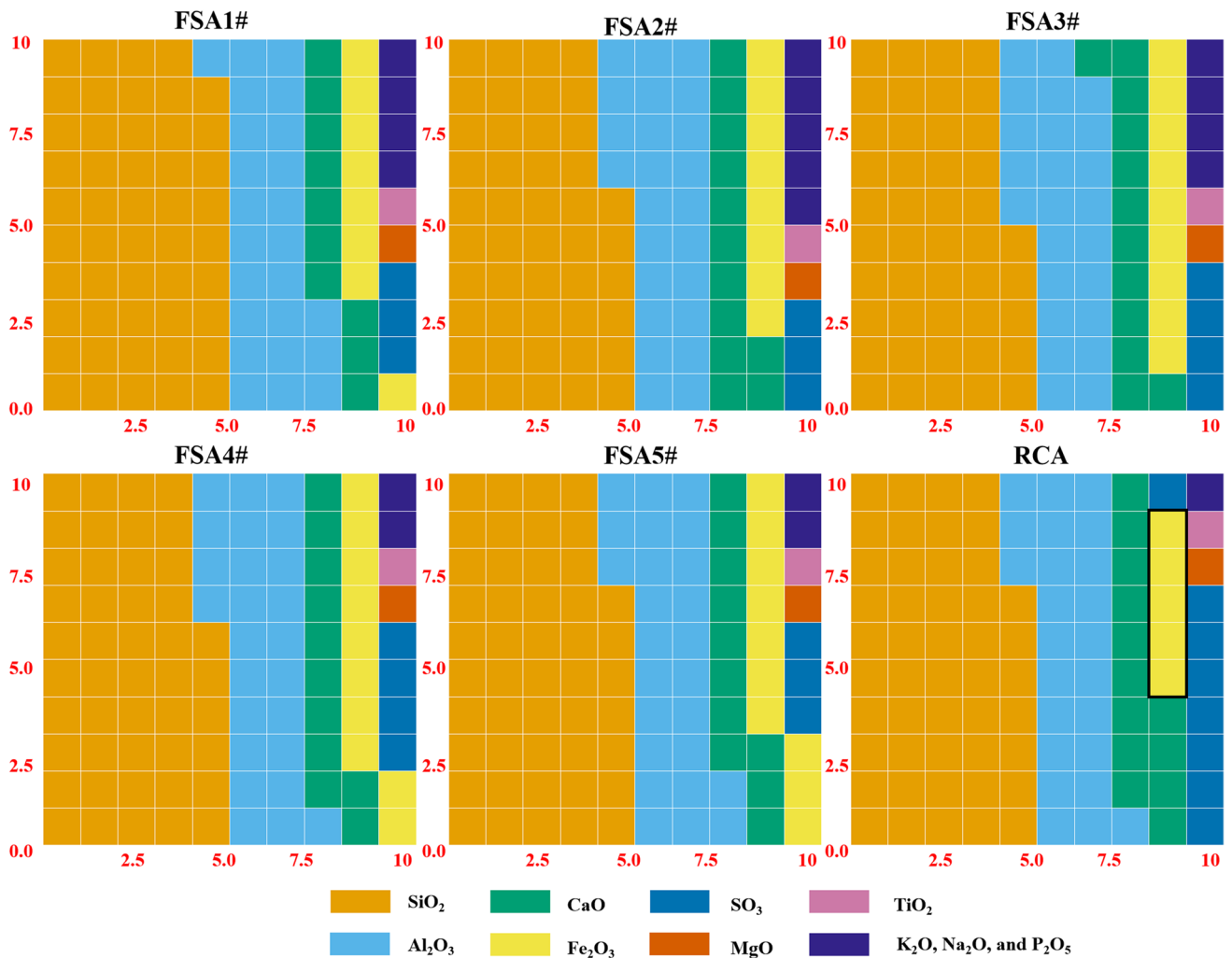
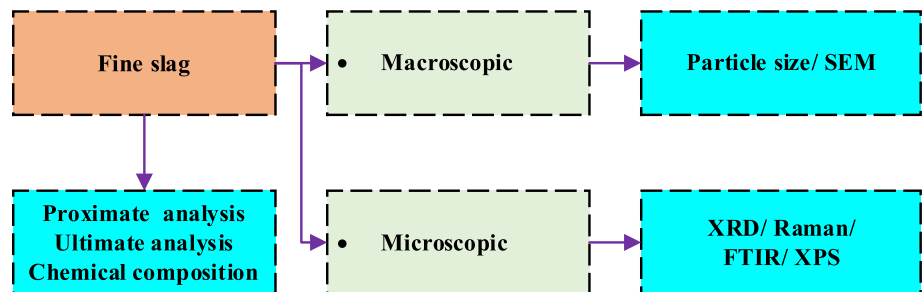


Fig. 2 Chemical composition of FSA and RCA

Fig. 3 Experimental flow chart



2.2.2 Microscopic characterization

The crystal mineral compositions of the FS and FSA were analyzed by X-ray diffraction (XRD, Ultima IV, Neo-Confcianism Corporation, Japan). Samples were scanned in the 2θ range of 15° – 80° with a step size of 0.02° and scanning speed of $2^{\circ}/\text{min}$ using Cu K α radiation ($\lambda = 0.15406 \text{ nm}$).

The carbon structure was analyzed by Raman spectroscopy (Raman, Renishaw-Invia, Renishaw, Britain). After further grinding, the samples were placed into the sample table. A 532-nm laser was used for excitation to scan the samples in the range of 800 – 2000 cm^{-1} .

The functional groups in the FS were analyzed by Fourier transform infrared (FTIR, Nicolet iS50, Thermo Fisher

Scientific, The United States) spectroscopy. Spectra were obtained in the range of 400–2000 cm^{-1} , and most bands were observed in the mid-infrared region of the spectra, corresponding to inorganic functional groups. The samples were prepared in the form of KBr pellets, with a sample to KBr mass ratio of 1:100.

The surface elements were investigated by X-ray photoelectron spectroscopy (XPS, Thermo Scientific K-Alpha, The United States), using Al $K\alpha$ radiation ($HV = 1486.6 \text{ eV}$) as the excitation source. Full-spectrum scanning was performed at a pass energy of 100 eV and step size of 1 eV. Narrow-spectrum scanning was performed at a pass energy of 50 eV and step size of 0.1 eV.

3 Results and discussion

3.1 Geometrical dimensions of FS at a macroscopic scale

The particle size of the pretreated FS was analyzed, and the results are shown in Fig. 4 and Table 2. All the three types of FS exhibited the characteristic “three-peak distribution,” although it was the most prominent for FS3#. This indicated a certain coherence for FS formation. The overall particulate size ranged from 0.5 to 350 μm . The first, second, and

third peaks ranged from 0.5 to 5 μm , 5 to 40 μm , and 40 to 350 μm , respectively, with the particle sizes of the samples overlapping.

In Figs. 5, 6, and 7, the local areas were randomly chosen to determine the global particle statistics. The particle sizes varied and were scattered throughout this region. The macrostructure of the FS produced was divided into two main categories. In the first category, single spherical particles of various sizes were observed—the largest spherical particle diameters in Figs. 5, 6, and 7 were approximately 45, 45, and 63 μm , respectively.

Figure 8 shows SEM images at various magnifications. A-1 and B-1 show bulk particles with sizes ranging from 200 to 300 μm . In A-2, A-3, B-2, and B-3, the surface contained cracks or holes of various sizes, and the surface crack was more significant. Many small irregular and spherical particles were attached onto the particle surface through both physical adsorption and engraving.

C-1 and D-1 show dense particles. Images C-2, C-3, D-2, and D-3 obtained at higher magnifications show that the surfaces contained cracks or folds and were relatively smooth. Compared with A-1 and B-1, the amount of particulate matter attached to the surface was significantly less.

The particulates shown in E-1 are porous and irregular. The corresponding higher-magnification images (E-2 and E-3) show many pores of various sizes on the surface. While the particles in E-1 had the same porosity characteristics as those in A-1 and B-1, there were no small charged particles

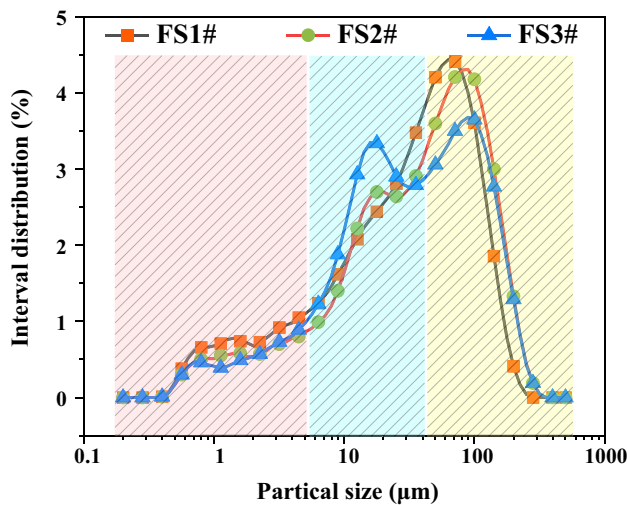


Fig. 4 Particle size distribution curves

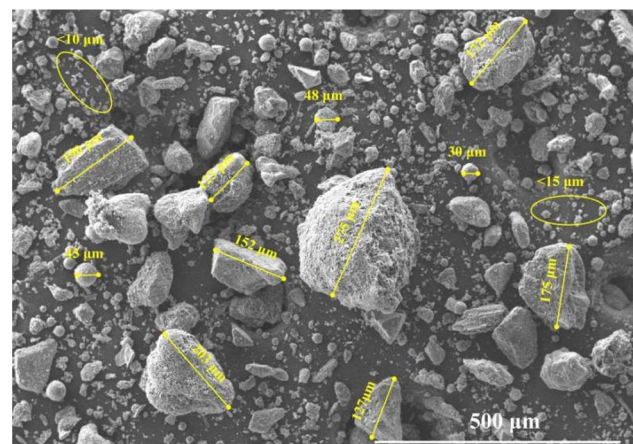


Fig. 5 Overall particle size distribution in FS1#

Table 2 Particle size distribution parameters

Samples	D3	D6	D10	D16	D25	D50*	D75	D84	D90	D97	D100
FS1#	0.983	1.578	2.974	5.901	11.84	36.22	73.54	93.73	112.4	155.6	274.3
FS2#	1.143	2.118	4.256	8.786	15.27	43.74	91.80	117.7	142.3	197.8	347.2
FS3#	1.220	2.475	4.656	8.394	13.38	33.92	85.39	113.2	139.4	196.8	347.2

*Repeatability limit < 1% (D50)

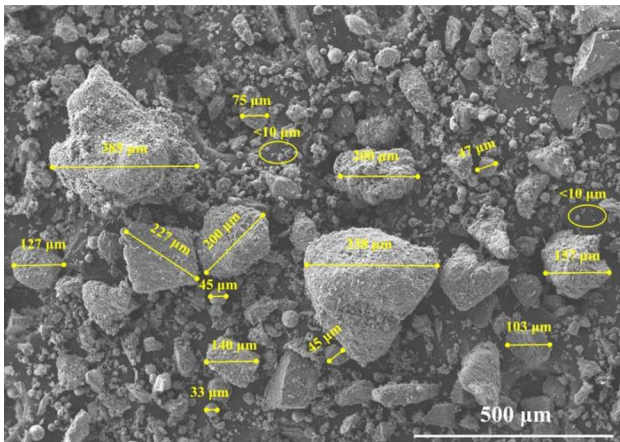


Fig. 6 Overall particle size distribution in FS2#

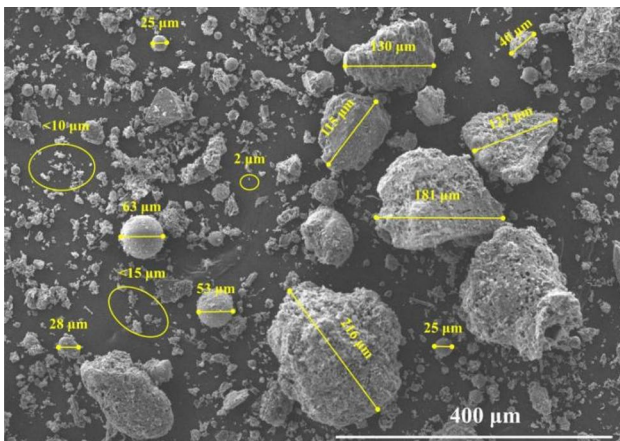


Fig. 7 Overall particle size distribution in FS3#

on their surfaces. Small particles were physically attached to such particles, and the attached particles were dispersed by vibration during the pretreatment process.

Images F-2, F-3, G-2, and G-3 show visible fold patterns on the surfaces. The overall particles in F-3 appear folded, whereas the localized particles in G-3 appear folded, with some small irregular as well as spherical particles embedded in the fold. Crinkled particles can be formed due to cracks in high-temperature coal particles. Such particles have small local cracks that expand into larger cracks. In conclusion, the number and size of the spherical particles attached to the surface and the pore structure of irregular particles are significantly different because of the different structures of the irregular particle matrix. The formation process of FS is related to particle breakage, ash accumulation, and slag deposition, and hence, FS with different particle sizes may have different characteristics.

Figure 9 shows the morphology of the fine particles, whose size was less than 40 μm. The smaller particles (<5 μm) were attached to their periphery or surface.

In Fig. 9, the irregular particles in the images are either dense particles (I-1 and I-5), or cracked particles (I-4 and I-6), or a combination of acicular particles, floc particles, and glitter particle (I-2 and I-3). The primary sources were tiny particles of unreacted or partially reacted raw coal and the reactions during the gasification process.

Images S-1 to S-6 show spherical particles of different diameters. Large spherical particles were not smooth, and some spherical particles had a rough surface (S-1, S-2, and S-4). Certain smooth surfaces were scattered with patches of various sizes (S-3). The spherical particles also had partial depressions (S-3) or the precursors (S-5) on the surface, indicating that the spherical particles were not formed directly but were formed through specific physical and chemical reactions.

3.2 Characteristics of the carbon-containing components at the microscopic scale

Figure 10 shows the XRD patterns of the FS. There was no obvious signal of mineral diffraction from the FS. Peak 002 (approximately 25°) and peak 100 (approximately 45°) in the diffraction pattern indicate a graphite-like structure in the FS. During gasification, the working temperature was higher than the melting temperature of the coal ash. Consequently, the mineral melted into a glassy material consisting mainly of fused silicate and aluminum silicate. After fast cooling, the slag did not exhibit a high degree of crystallinity and formed more amorphous components.

Raman spectroscopy is an effective technique for characterizing the structure of carbon owing to the sensitivity of Raman signals to crystalline and amorphous structures. Figures 11a, b, and c shows characteristic bands at approximately 1350 cm^{-1} (peak D) and 1590 cm^{-1} (peak G) (Yu 2021). Deconvolution of the spectra showed five peaks (G, D1, D2, D3, and D4). Peak G corresponds to an orderly network of graphitic carbon. Peak D1 (1350 cm^{-1}) corresponds to a more extensive aromatic nucleus system related to edges or other defects (such as edge carbon atoms or heteroatoms) and originates from the vibrations in the isolated sp^2 hybrid bond planes. Peak D2 (1620 cm^{-1}) appears simultaneously with peak D1, reflecting the vibration mode of the graphite lattice with E_{2g} symmetry. Peak D3 (1520 cm^{-1}) can be attributed to a minor aromatic nucleus system in the aromatic structural unit, corresponding to the sp^2 hybrid structure of amorphous carbon in the organic molecule or functional groups. Peak D4 (1200 cm^{-1}) is usually observed for combined polyene structure with sp^2 – sp^3 hybrid systems owing to crystallite edges or combined C=C and C–C bonds,

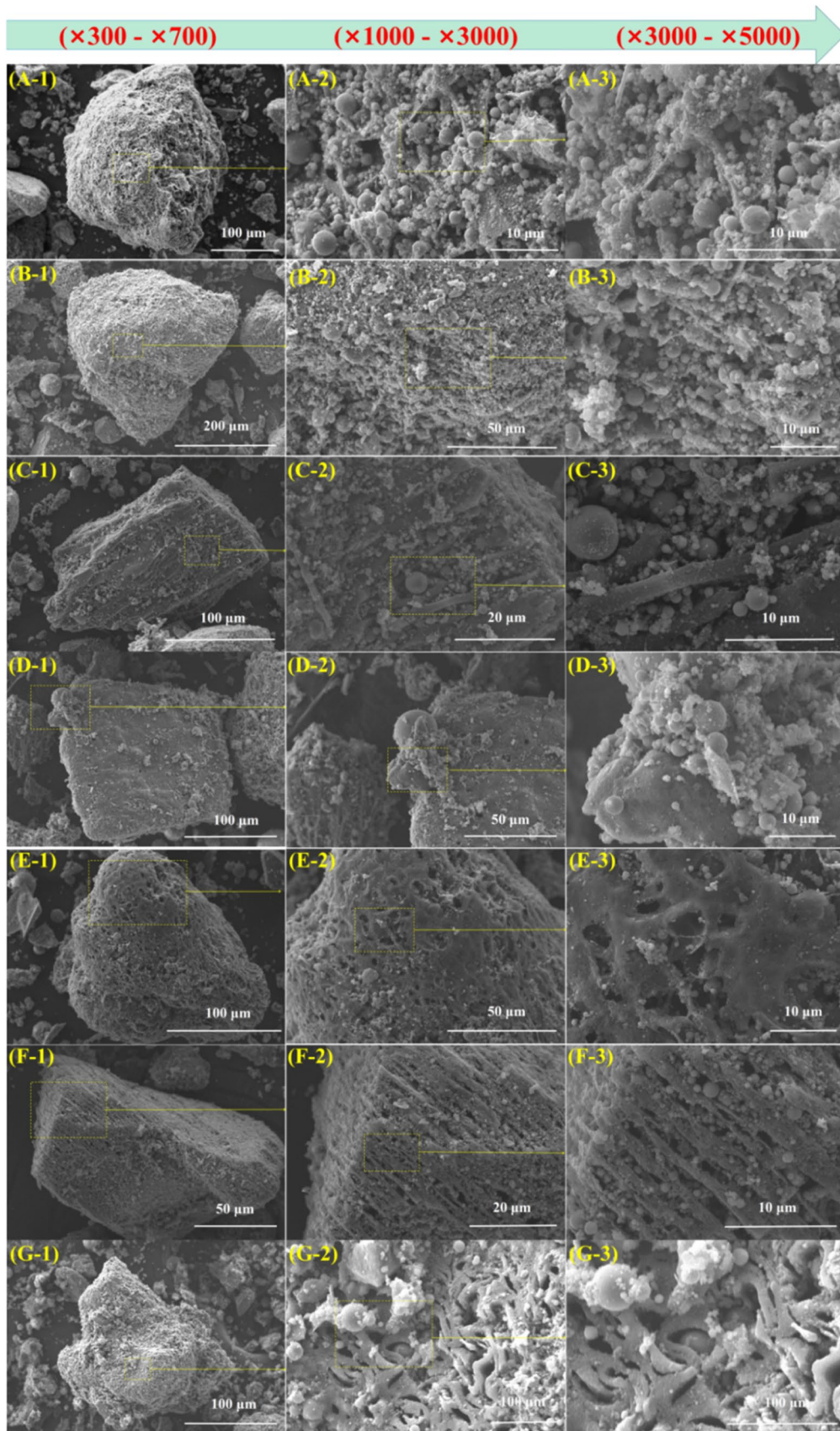


Fig. 8 Apparent particle morphology at different magnifications

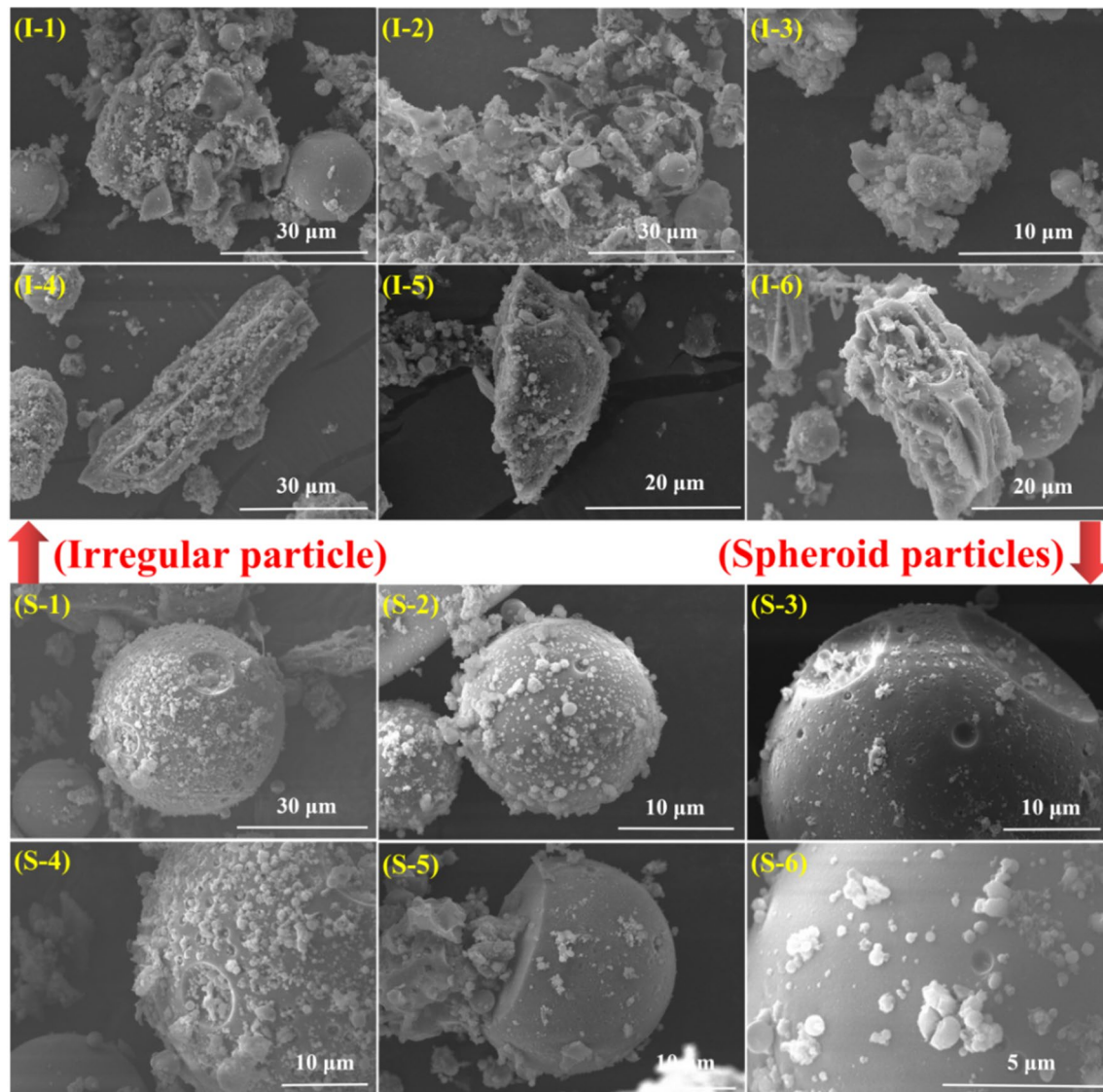


Fig. 9 Apparent morphology of particles with sizes less than 40 μm

typically representing the active site, reactive site, and cross-linking structure (Xu 2021; Wu 2014).

The A_{D3+D4}/A_{All} ratio represents the number of reaction sites on the carbon structure. The A_{D1}/A_G and A_G/A_{All} ratios represent the magnitude of the carbon structure, and the $A_{D3}/A_{G+D2+D3}$ ratio represents the amount of amorphous carbon structure. The proportions of these structures are shown in Fig. 11d. According to the fitted peak areas, the areas decrease in the order $A_{D1} > A_{D3} > A_{D4} > A_G > A_{D2}$. The highest area of peak D1 implies a high number of aromatic nuclei, mainly from the graphite structure, with a more intense aromatic structure. This peak D3 originates primarily from the hybrid sp^2 structure of amorphous carbon. Peak D4 reflects the presence of some active sites, indicating that the carbon structure still has specific reactivity. The active

sites were derived from the original coal particles that did not respond completely to the gasification process. According to the A_{D3+D4}/A_{All} and $A_{D3}/A_{G+D2+D3}$ ratios, the number of reaction sites in FS1#, caused by the carbon structure, was higher. Fundamental analysis revealed that FS1# has more volatiles. The A_{D1}/A_G and A_G/A_{All} ratios indicate that FS2# and FS3# have a higher-order structure compared to FS1#. The more the number of reactive sites on amorphous carbon, the limited will be the consumption or transformation in carbon gasification, and higher will be the amount of carbon structures preserved in the FS (Guo 2022). It is evident that the structure of the residual carbon in FS has specific commonalities. This is directly related to the nature of the raw coal and the course of the reaction owing to the difference in the degree of crystallinity.

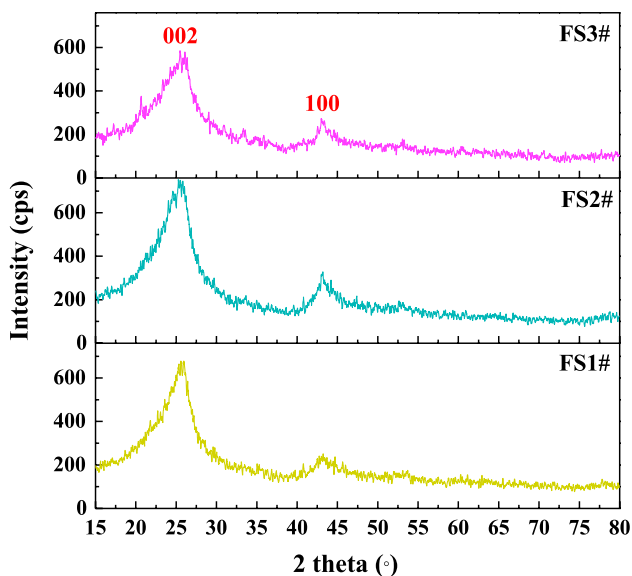


Fig. 10 XRD patterns of the FS

XPS is used to determine the elemental composition, chemical state, and electronic state of materials (Perry and Grint 1983). The C 1s XPS spectrum ranges from 281 to 292 eV. The carbon on the FS surface consists of five components. The C–C and C–H peaks appeared at 284.8 eV, while hydroxyl/ether (C–O), carbonyl (C=O), carboxyl (COO⁻), and π–π* peaks appeared at 285.4 ± 0.2 eV, 287.5 ± 0.2 eV, 289.0 ± 0.2 eV, and 291.5 ± 0.2 eV 3233, respectively. The peak at 294.3 eV can be attributed to the

oscillations involving π–π* excitation in unsaturated and aromatic species (Pantea 2003; Kozowski 2004). The peak deconvolution is shown in Fig. 12.

The peaks were fitted to obtain the area under the peak, and the ratios of the different peak areas were obtained (Fig. 12d). The proportion of aromatic C–C or C–H bonds on the surface of the FS was the highest. Carbon primarily formed a single bond (hydroxyl or ether), although small amounts of double bonded carbon (as C=O and COO⁻ groups) were also present. In raw coal, most C=O and COO⁻ bonds dissociate after the various high-temperature processes. At elevated temperatures, the C–O groups in phenol, alcohol, or other compounds formed are easily dissociated. This is probably because the residual C–O groups did not react entirely with the raw coal particles; a portion of these groups is present in the carbonate structure of the inorganic components (Miao 2020a, b, c; Li 2021; Xie 2016).

On the one hand, coal particles undergo complex reactions in the gasifier, in which the carbon structure will change under the influence of temperature. On the other hand, the residual carbon in the FS may be formed when the coal particles in the gasifier do not reach the required conditions for a complete reaction or need more reaction time. Carbon-containing components' bond binding and occurrence forms show relatively consistent characteristics. Although there are minor differences, the degree of common traits is far greater than the differences. According to Raman results, the area of peaks D3 and D4 in F1# is more significant, which reflects the higher content of the hybrid sp² structure of amorphous carbon and crystal edge or the

Fig. 11 Raman spectra and composition of FS

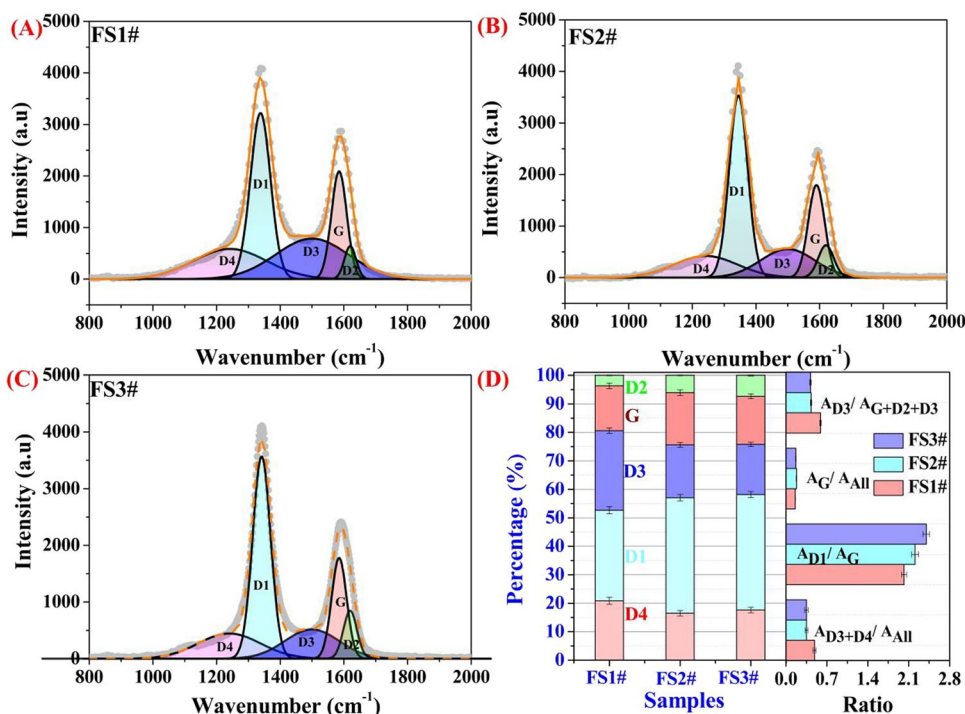
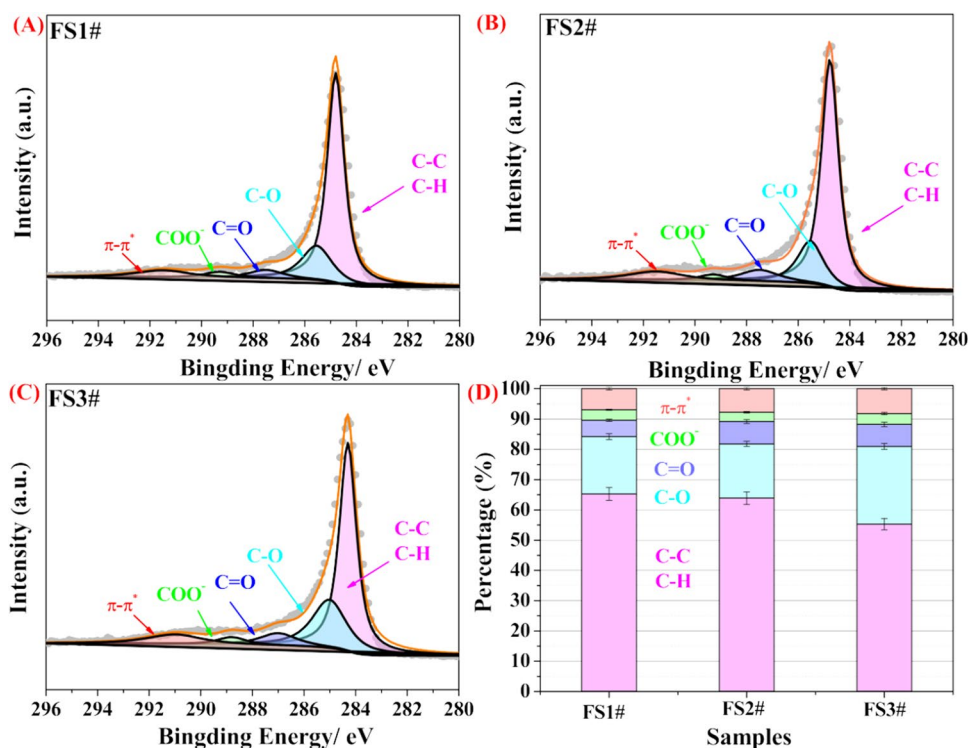


Fig. 12 Fitted peaks and parameters of the C 1s spectrum of FS



combination of $\text{C}=\text{C}$ and $\text{C}-\text{C}$ bonds. In XPS results, there are relatively more $\text{C}-\text{C}$ bonds in F1#. These results indicate that FS1# has more reaction sites and cross-linking structures than FS2# and FS3#.

3.3 Characteristics of the inorganic components at a microscopic scale

To understand the primary crystalline forms of FSA, the mineral composition of the crystals of various FSA was analyzed by XRD. The XRD patterns are shown in Fig. 13. The spectra of the three FSA are basically the same, indicating common features of the slag after combustion. The prominent peaks correspond to hematite (Fe_2O_3), anhydrous gypsum (CaSO_4), and mullite ($\text{Al}_6\text{Si}_2\text{O}_{13}$). Clusters of peaks were detected at a 2θ value of 25° . The FSA contained a certain amount of amorphous inorganics. Combining with the XPS results, it was concluded that the amorphous structures contained silicon, aluminum, iron, and calcium (Zhang 2019).

The FTIR spectrum was not affected by the crystalline structure of the mineral constituents. However, there were numerous amorphous mineral components in the FS obtained under the high-temperature atmosphere of the gasifier. A portion of the mid-infrared region ($400\text{--}2000\text{ cm}^{-1}$) was selected for the experiment. Figure 14 shows the spectra of the three types of FS. The spectra of the three FS were similar. Thus, all the FS have similar functional groups, although there are minor differences.

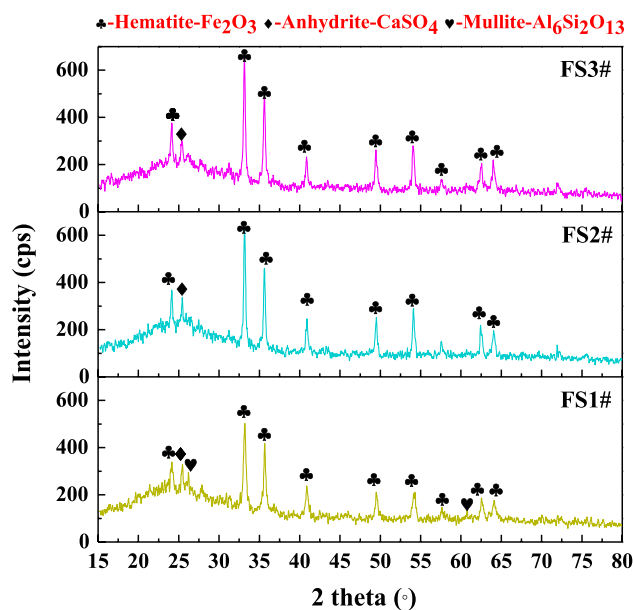


Fig. 13 Mineral composition of the FSA

Bands at 1585 and 1641 cm^{-1} can be attributed to aromatic $\text{C}=\text{C}$ stretching vibrations of graphite carbon. The FS has a particular aromatic structure about the residual carbon (Guo 2020). The bands from 1138 to 1009 cm^{-1} are asymmetrical, corresponding to $\text{Si}-\text{O}-\text{Si}$. The spectra showed a weak shoulder at $710\text{--}770\text{ cm}^{-1}$, attributable to the stretching vibration of $\text{Si}-\text{O}-\text{Al}$ (720 cm^{-1}) and symmetrical

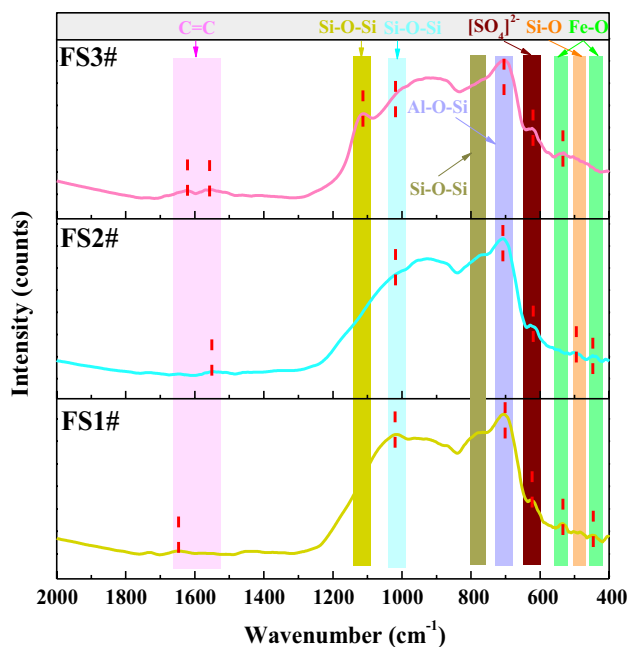


Fig. 14 FTIR spectra of FS

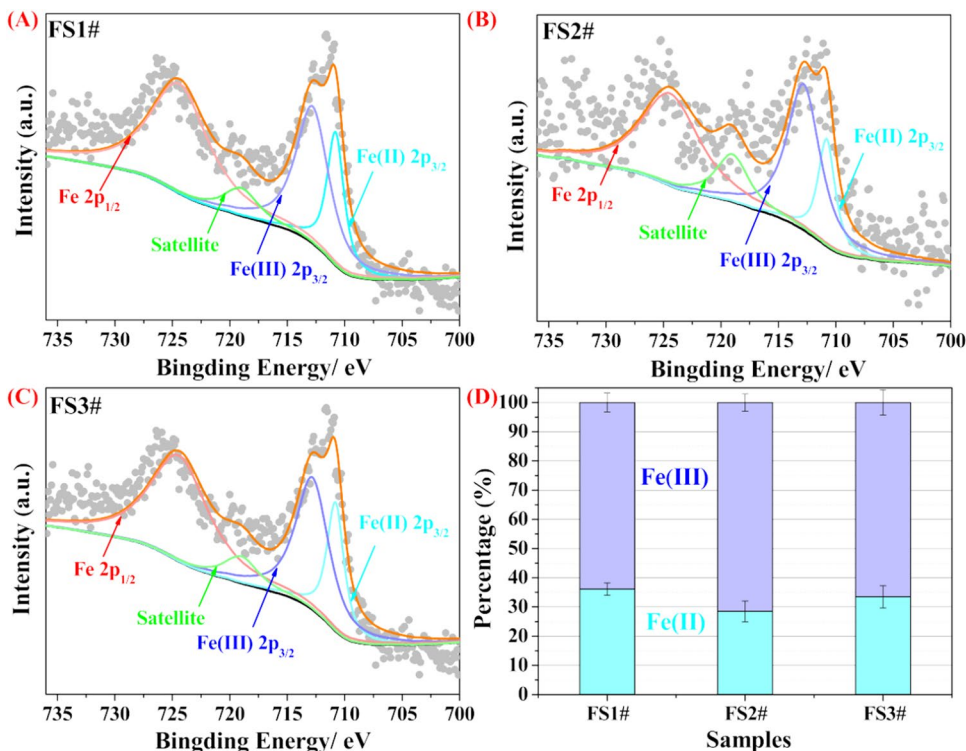
stretching vibration of Si–O–Si (770 cm^{-1}). The signal from the Si–O flexural vibration in quartz appeared at 470 cm^{-1} in the spectra (Zhao 2021; Mozgawa 2014). The bands from 1138 to 1009 cm^{-1} are asymmetrical, corresponding to Si–O–Si. The spectra showed a weak shoulder at

$710\text{--}770\text{ cm}^{-1}$, attributable to the stretching vibration of Si–O–Al (720 cm^{-1}) and symmetrical stretching vibration of Si–O–Si (770 cm^{-1}). The signal from the Si–O flexural vibration in quartz appeared at 470 cm^{-1} in the spectra (Lin 2012). The peak at 612 cm^{-1} mainly originated from the in-plane bending vibration of SO_4^{2-} and could be attributed to the molecular vibration of anhydrite (Yin 2018). The FTIR spectra of FS showed an obvious peak for the Fe–O bond and a specific vibrational stretching pattern near 452 and 565 cm^{-1} (Chen 2017; Yadav 2020).

As shown in Fig. 2, there was an obvious enrichment of elemental Fe. XPS was used to further analyze the oxidation state of iron in Fig. 15. The Fe $2p_{1/2}$ and Fe $2p_{3/2}$ peak positions depend on the ionic state of Fe. The satellite peaks of Fe $2p_{1/2}$ and Fe $2p_{3/2}$ are also dependent on the oxidation state and have been used to qualitatively determine the oxidation state of iron ions.

In the high-resolution Fe $2p$ spectrum, peaks appeared at $724.4 \pm 0.2\text{ eV}$ (Fe $2p_{1/2}$) and $710.8 \pm 0.2\text{ eV}$ (Fe $2p_{3/2}$). The satellite signal appeared at $719.2 \pm 0.2\text{ eV}$ and typically indicates the transformation of FeO (Fe^{2+}) to Fe_3O_4 and Fe_2O_3 (Fe^{3+}) to Fe_3O_4 . Meanwhile, the Fe $2p_{3/2}$ peak can be deconvoluted into Fe(III) peak at $711.0 \pm 0.2\text{ eV}$ and Fe(II) peak at $713 \pm 0.2\text{ eV}$ (Yang 2015; Ai 2013). The specific peak fitting results are shown in Fig. 15A, B, and C. Iron compounds can be either high-spin or low-spin (as defined by the crystal field theory). The spin of Fe(III) compounds always increases, leading to complex multiple-peak Fe $2p$

Fig. 15 Peak fitting of the Fe $2p$ XPS spectrum and composition of Fe in the FS



spectra. Fe(II) compounds may have high or low spin (Biesinger 2011).

Figure 15d shows the percentage areas of Fe(II) and Fe(III). Fe mainly exists in the form of Fe(III). The crystalline mineral composition of FSA reveals the presence of hematite with trivalent iron. Simultaneously, oxides containing divalent iron or other inorganic minerals can be fused with elements such as silicon and aluminum. The form of iron in the FS can change during the gasification reaction, although there are some common features. The state of Fe in the FS still requires investigation.

It can be seen that both crystal mineral composition and chemical bond display relatively consistent characteristics. While there are minor differences, the degree of common traits is far greater than the differences. There are two main reasons for the difference: (1) The production of FS is directly related to the actual operation condition and is subject to the temperature, pressure and the properties of the raw coal in the furnace; (2) The FS mainly contains inorganic and carbon-containing components, among which there is a specific occurrence relationship between carbon and ash. The difference may be due to the difference in carbon-containing components.

Figure 16 summarizes the partial characteristics of the FS at different scales. The FS primarily contains large amounts of inorganic and carbon components. Macroscopically, FS exhibits a characteristic "three-peak distribution." FS particles exhibit regular spheroidal particles and irregular particles. Microscopically, the carbon structure has a certain degree of order. C 1s contains many aromatic structures. FS contains a vitreous inorganic component. The inorganic components are primarily silicon, aluminum, iron, and

calcium. Inorganic components mainly contain Si–O–Si, Si–O–Al, Si–O, SO_4^{2-} , and Fe–O bonds.

4 Conclusions

In conclusion, certain properties, such as particle size distribution, composition, crystalline structure, and valence binding, were common in the FS. The reaction of coal in the gasifier is complex, and the FS in the Shell gasifier has specific differences, although many common characteristics can be observed. The FS primarily contains large amounts of inorganic and carbon components. The inorganic components were mainly silicon, aluminum, iron, and calcium. Macroscopically, FS exhibits a characteristic "three-peak distribution." Microscopically, the carbon structure has a certain degree of order. C 1s contains many aromatic structures, and $A_{\text{C-C\&C-H}} > A_{\text{C-O}} > A_{\pi-\pi^*} > A_{\text{C=O}} > A_{\text{COO}^-}$. FS contains a vitreous inorganic component. The inorganic components are primarily silicon, aluminum, iron, and calcium, with a total content of more than 90%. Inorganic components mainly contain Si–O–Si, Si–O–Al, Si–O, SO_4^{2-} , and Fe–O bonds. Particularly, Fe mainly exist in the form of Fe(III), and the Fe 2p spectrum can be deconvoluted into Fe 2p_{1/2}, Fe 2p_{3/2}, and satellite peaks. To develop efficient coal gasification technologies, the training and removal of FS would be a critical research direction in the future. The findings of this study will be beneficial in many aspects. The utilization of FS resources will differ based on the composition and properties. The qualitative use of FS can be better realized after the characteristics of the different components are identified. The mineral composition, inorganic functional groups on the surface of FS, and the structural characteristics of C and Fe

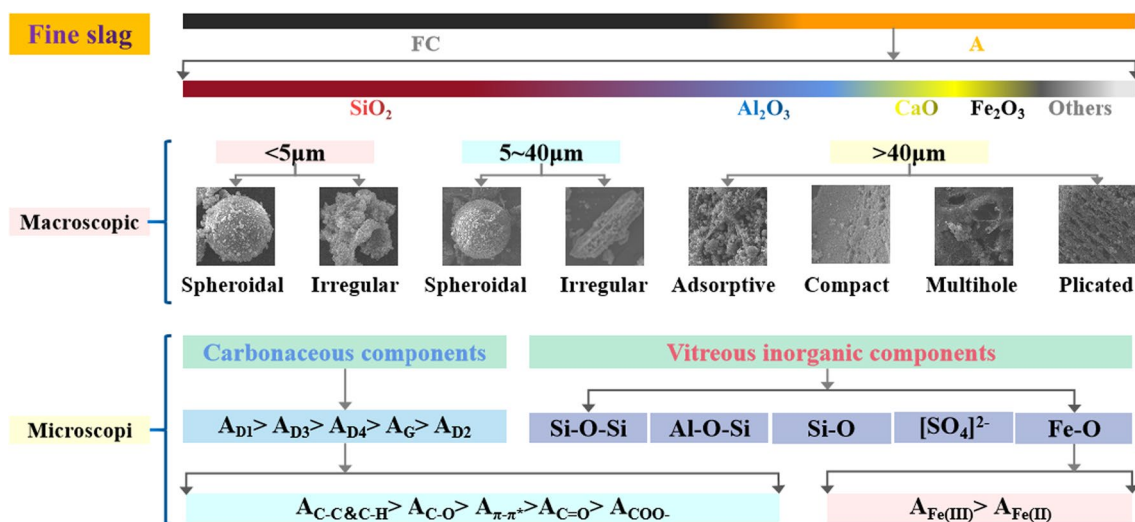


Fig. 16 Analysis of partial characteristics of FS at different scales

revealed in this study will be beneficial for elucidating the formation process of FS.

Acknowledgements The completion of this work and related results received support from the Scientific Research Foundation for the Introduction of Talent in Anhui University of Science and Technology (2023yjrc90), the Graduate Research Project of Higher Education in Anhui Province (YJS20210377), the Postgraduate Innovation Fund of Anhui University of Science and Technology (2021CX1002), the University Synergy Innovation Program of Anhui Province (GXXT-2020-006), and the National Science Fund for Young Scientists (52200139).

Author contributions LM: Conceptualization, methodology, data curation, writing—original draft. MZ: Conceptualization, supervision. BX: Methodology. FJ: Methodology. TL: Methodology. YZ: Methodology. ST: Methodology. HL: Conceptualization, supervision.

Declarations

Conflict of interest The authors declare that they have no known competing financial interests or personal relationships that could have appeared to influence the work reported in this paper.

Open Access This article is licensed under a Creative Commons Attribution 4.0 International License, which permits use, sharing, adaptation, distribution and reproduction in any medium or format, as long as you give appropriate credit to the original author(s) and the source, provide a link to the Creative Commons licence, and indicate if changes were made. The images or other third party material in this article are included in the article's Creative Commons licence, unless indicated otherwise in a credit line to the material. If material is not included in the article's Creative Commons licence and your intended use is not permitted by statutory regulation or exceeds the permitted use, you will need to obtain permission directly from the copyright holder. To view a copy of this licence, visit <http://creativecommons.org/licenses/by/4.0/>.

References

- Ai Z (2013) Core-shell structure dependent reactivity of Fe@Fe₂O₃ nanowires on aerobic degradation of 4-chlorophenol. *Environ Sci Technol* 47:5344–5352. <https://doi.org/10.1021/es4005202>
- Biesinger M (2011) Resolving surface chemical states in XPS analysis of first row transition metals, oxides and hydroxides: Cr, Mn, Fe, Co and Ni. *Appl Surf Sci* 257(7):2717–2730. <https://doi.org/10.1016/j.apsusc.2010.10.051>
- Cao J (2021) Current status of hydrogen production in China. *Prog Chem* 33(12):2215–2244. <https://doi.org/10.7536/PC201128>
- Chai S (2021) Industrial hydrogen production technology and development status in China: a review. *Clean Technol Environ* 23(7):1931–1946. <https://doi.org/10.1007/s10098-021-02089-w>
- Chen Z (2017) Synthesis of magnetic Fe₃O₄/CFA composites for the efficient removal of U(VI) from wastewater. *Chem Eng J* 320:448–457. <https://doi.org/10.1016/j.cej.2017.03.074>
- China Government Network (2021) Xi Jinping attended the general debate of the 76th UN General Assembly and delivered an important speech. https://www.gov.cn/xinwen/2021-09/22/content_5638597.htm
- Ding L, Yang M, Dong K, Vo DVN, Hungwe D, Ye J, Ryzhkov A, Yoshikawa K (2022) Mobile power generation system based on biomass gasification. *Int J Coal Sci Technol* 9(1):34. <https://doi.org/10.1007/s40789-022-00505-0>
- Guo X (2020) Evaluation of carbon forms and elements composition in coal gasification solid residues and their potential utilization from a view of coal geology. *Waste Manag* 114:287–298. <https://doi.org/10.1016/j.wasman.2020.06.037>
- Guo Y (2022) Comparative study on the structure characteristics, combustion reactivity, and potential environmental impacts of coal gasification fine slag with different particle size fractions. *Fuel* 311:122493. <https://doi.org/10.1016/j.fuel.2021.122493>
- Kozowski M (2004) XPS study of reductively and non-reductively modified coals. *Fuel* 83(3):259–265. <https://doi.org/10.1016/j.fuel.2003.08.004>
- Krishnamoorthy V (2017) A study on fragmentation behavior, inorganic melt phase formation, and carbon loss during high temperature gasification of mineral matter rich fraction of Pittsburgh No. 8 coal. *Fuel* 208:247–259. <https://doi.org/10.1016/j.fuel.2017.06.134>
- Li J (2021) Effects of flotation and acid treatment on unburned carbon recovery from atmospheric circulating fluidized bed coal gasification fine ash and application evaluation of residual carbon. *Waste Manag* 136:283–294. <https://doi.org/10.1016/j.wasman.2021.10.024>
- Lin X (2012) Correlation between fluidity properties and local structures of three typical Asian coal ashes. *Energy Fuels* 26(4):2136–2144. <https://doi.org/10.1021/ef201771f>
- Liu X (2021) Review of the characteristics and graded utilisation of coal gasification slag. *Chin J Chem Eng* 35:92–106. <https://doi.org/10.1016/j.cjche.2021.05.007>
- Lv P (2021) Investigation into the catalytic gasification of coal gasification fine slag residual carbon by the leachate of biomass waste: Gasification reactivity, structural evolution and kinetics analysis. *J Environ Chem Eng* 9:106715. <https://doi.org/10.1016/j.jece.2021.106715>
- Miao Z (2020a) Physicochemical characteristics of mineral-rich particles present in fine slag from entrained-flow gasifiers. *Energy Fuels* 34(1):616–623. <https://doi.org/10.1021/acs.energyfuels.9b02732>
- Miao Z (2020b) Chemical characterizations of different sized mineral-rich particles in fine slag from entrained-flow gasification. *Adv Powder Technol* 31(9):3715–3723. <https://doi.org/10.1016/j.appt.2020.07.010>
- Miao Z (2020c) Physical properties and microstructures of residual carbon and slag particles present in fine slag from entrained-flow coal gasification. *Adv Powder Technol* 31(9):3781–3789. <https://doi.org/10.1016/j.appt.2020.07.019>
- Mozgawa W (2014) Investigation of the coal fly ashes using IR spectroscopy. *Spectrochim Acta A* 132:889–894. <https://doi.org/10.1016/j.saa.2014.05.052>
- Pan C (2016) Characteristics of different sized slag particles from entrained-flow coal gasification. *Energy Fuels* 30(2):1487–1495. <https://doi.org/10.1021/acs.energyfuels.5b01326>
- Pantea D (2003) Electrical conductivity of conductive carbon blacks: influence of surface chemistry and topology. *Appl Surf Sci* 217(1):181–193. [https://doi.org/10.1016/S0169-4332\(03\)00550-6](https://doi.org/10.1016/S0169-4332(03)00550-6)
- Perry D, Grint A (1983) Application of XPS to coal characterization. *Fuel* 62(9):1024–1033. [https://doi.org/10.1016/0016-2361\(83\)90135-7](https://doi.org/10.1016/0016-2361(83)90135-7)
- Shen Z (2021) A deep insight on the coal ash-to-slag transformation behavior during the entrained flow gasification process. *Fuel* 289:119953. <https://doi.org/10.1016/j.fuel.2020.119953>
- Smolinski A, Wochna S, Howanec N (2022) Gasification of lignite from Polish coal mine to hydrogen-rich gas. *Int J Coal Sci Technol* 9(1):77. <https://doi.org/10.1007/s40789-022-00550-9>

- Troiano M (2018) Modelling entrained-flow slagging gasification of solid fuels with near-wall particle segregation. *Chem Eng J* 377:119962. <https://doi.org/10.1016/j.cej.2018.09.123>
- Wang F (2021a) Opposed multi-burner gasification technology: recent process of fundamental research and industrial application. *Chin J Chem Eng* 35:124–142. <https://doi.org/10.1016/j.cjche.2021.07.007>
- Wang H (2021b) Melting characteristics of coal ash and properties of fly ash to understand the slag formation in the Shell gasifier. *ACS Omega* 6(24):16066–16075. <https://doi.org/10.1021/acsomega.1c01949>
- Wu S (2014) Structure characteristics and gasification activity of residual carbon from entrained-flow coal gasification slag. *Fuel* 122:67–75. <https://doi.org/10.1016/j.fuel.2014.01.011>
- Wu S (2015) Characteristics and catalytic actions of inorganic constituents from entrained-flow coal gasification slag. *J Energy Inst* 88(1):93–103. <https://doi.org/10.1016/j.joei.2014.04.001>
- Xie W (2016) Characterization of hydrogenated graphite powder by X-ray photoelectron spectroscopy and time-of-flight secondary ion mass spectrometry. *RSC Adv* 6(84):80649–80654. <https://doi.org/10.1039/C6RA17954A>
- Xu S (2009) The gasification reactivity of unburned carbon present in gasification slag from entrained-flow gasifier. *Fuel Process Technol* 90(9):1062–1070. <https://doi.org/10.1016/j.fuproc.2009.04.006>
- Xu J (2021) Developing micro-Raman spectroscopy for char structure characterization in the scale of micro- and bulk: a case study of Zhundong coal pyrolysis. *Fuel* 291:120168. <https://doi.org/10.1016/j.fuel.2021.120168>
- Yadav V (2020) A novel synthesis and characterization of polyhedral shaped amorphous iron oxide nanoparticles from incense sticks ash waste. *Environ Technol Inno* 20:101089. <https://doi.org/10.1016/j.eti.2020.101089>
- Yang L (2015) Heterogeneous degradation of organic pollutants by persulfate activated by CuO–Fe₃O₄: mechanism, stability, and effects of pH and bicarbonate ions. *Environ Sci Technol* 49(11):6838–6845. <https://doi.org/10.1021/acs.est.5b00623>
- Yang Q (2022) Pathways toward carbon-neutral coal to ethylene glycol processes by integrating with different renewable energy-based hydrogen production technologies. *Energy Convers Manag* 258:115529. <https://doi.org/10.1016/j.enconman.2022.115529>
- Yin Y (2018) Characterization of mineral matter in coal ashes with Infrared and Raman spectroscopy. *Spectrosc Spectral Anal* 38(3):789–793. [https://doi.org/10.3964/j.issn.1000-0593\(2018\)03-0789-05](https://doi.org/10.3964/j.issn.1000-0593(2018)03-0789-05)
- Yu J (2021) Study on the effect of inherent AAEM on char structure evolution during coal pyrolysis by in-situ Raman and TG. *Fuel* 292:120406. <https://doi.org/10.1016/j.fuel.2021.120406>
- Zhakupov D, Kulmukanova L, Sarbassov Y, Shah D (2022) Flue gas analysis for biomass and coal co-firing in fluidized bed: process simulation and validation. *Int J Coal Sci Technol* 9(1):59. <https://doi.org/10.1007/s40789-022-00531-y>
- Zhang Y (2019) Study on distribution, chemical states and binding energy shifts of elements on the surface of gasification fine ash. *Res Chem Intermed*. <https://doi.org/10.1007/s11164-019-03824-1>
- Zhao X (2010) The surface characteristics and reactivity of residual carbon in coal gasification slag. *Energy Fuels* 24(1):91–94. <https://doi.org/10.1021/ef9005065>
- Zhao X (2021) Effect and mechanisms of synthesis conditions on the cadmium adsorption capacity of modified fly ash. *Ecotox Environ Safe* 223(1):112550. <https://doi.org/10.1016/j.ecoenv.2021.112550>

Publisher's Note Springer Nature remains neutral with regard to jurisdictional claims in published maps and institutional affiliations.